



Cite this: *J. Mater. Chem. A*, 2024, **12**, 20107

Enhancing CO₂ hydrogenation to methanol via the synergistic effect of MoS₂ interlayer spacing and sulfur vacancies†

Langlang Qin,^a Yunfei Gao,^{id *b} Caiyun Han,^a Minghui Zhu,^{id d} and Shuang Wang,^{id *ac}

The hydrogenation of carbon dioxide (CO₂) to methanol is an important reaction to convert CO₂ into valuable products and reduce carbon emission. MoS₂ is an effective catalyst for CO₂ hydrogenation, but the synergistic effects of interlayer spacing expansion and surface sulfur vacancy strengthening have not been studied systematically. Here, this work reports hydrazine hydrate as an effective reducing agent for MoS₂. The reducing agent can not only expand the interlayer spacing of MoS₂, but also increase the concentration of sulfur vacancies through a simple treatment. More importantly, the synergistic effect between the interlayer spacing and sulfur vacancies of MoS₂ significantly increases the methanol space-time yield (STY). At 220 °C, 4 MPa, and 8000 mL g_{cat}⁻¹ h⁻¹, the MoS₂-N₂H₄-4 catalyst exhibits 76.8% methanol selectively, 5.52% CO₂ conversion, and a high methanol STY of up to 0.1214 g_{cat}⁻¹ h⁻¹ and lasts for at least 200 h. The structure–performance relationship was further studied using physiochemical characterization and DFT. These results provide valuable insights into the development of highly efficient MoS₂ catalysts for CO₂ hydrogenation.

Received 25th April 2024

Accepted 27th June 2024

DOI: 10.1039/d4ta02861a

rsc.li/materials-a

^aCollege of Environmental Science and Engineering, Taiyuan University of Technology, Jinzhong 030600, Shanxi, P. R. China. E-mail: wangshuang@tyut.edu.cn

^bInstitute of Clean Coal Technology, East China University of Science and Technology, Shanghai 200237, P. R. China. E-mail: yunfeigao@ecust.edu.cn

^cShanxi Key Laboratory of Gas Energy Efficient and Clean Utilization, Taiyuan University of Technology, Taiyuan 030024, Shanxi, P. R. China

^dState Key Laboratory of Chemical Engineering, School of Chemical Engineering, East China University of Science and Technology, Shanghai 200237, PR China

† Electronic supplementary information (ESI) available. See DOI: <https://doi.org/10.1039/d4ta02861a>



Yunfei Gao

Yunfei Gao has been a professor at the East China University of Science and Technology (ECUST) since 2021. He graduated from North Carolina State University with a Ph.D. in 2019, and Tsinghua University in China as a bachelor in 2014. His work is mainly focused on CO₂ utilization, hydrogen production and selective oxidative dehydrogenation of light alkanes using chemical looping technologies. He has published more than 40 papers in

Science Advances, Nat. Commun., Energy Environ. Sci. and many other top journals. He is currently the project leader of several National Science Foundation Programs of China.

1 Introduction

The rapid growth of the global economy has led to a large amount of carbon dioxide (CO₂) emission, which has destroyed the ecological balance and caused various environmental problems.^{1,2} However, CO₂ is also a cheap and readily available renewable carbon resource that can be converted into clean fuels and high-value chemical products (such as carbon monoxide, methanol, methane, *etc.*).^{3–5} Methanol exhibits favourable transportability and serves as fundamental feedstock for high-value chemicals (*e.g.*, olefins and aromatics) as well as fuels (*e.g.*, gasoline).^{6–8} Therefore, researchers have developed a strong interest in CO₂ hydrogenation to methanol. At present, the main catalysts developed for CO₂ hydrogenation to methanol are Cu–metal oxides,⁴ In₂O₃-based oxides,^{9,10} ZnO/ZrO₂-solid solution,¹¹ MoS₂,^{12,13} *etc.*

In recent years, molybdenum disulfide (MoS₂) has been explored in the process of CO₂ hydrogenation to methanol and has shown excellent performance.^{12–15} There is a strong structure–activity relationship between the morphology of MoS₂ and its CO₂ hydrogenation performance.^{16,17} For example, Deng *et al.* prepared few-layer MoS₂, which achieved a selectivity of 94.3% for methanol and a conversion of 12.5% of CO₂ at 180 °C, attributed to the exposure of more active sites in the few-layer structure.¹⁸ Zhou *et al.* developed boxlike assemblies of quasi-single-layer MoS₂ nanosheets (h-MoS₂/ZnS), and the space-time yield (STY) of CO₂ hydrogenation to methanol reached 0.93 g_{CH₃OH} g_{MoS₂}⁻¹ h⁻¹ at 260 °C.¹⁹ More importantly, highly

dispersed molybdenum disulfide nanosheets with fewer layers can promote the generation of abundant active sites. They discovered that CO_2 is decomposed into CO^* on MoS_2 , leading to improved selectivity of methanol.^{18,19} In addition to the few-layer structure of MoS_2 , sulfur vacancies also play a key role in its catalytic ability. Fei *et al.* found that the presence of Sv caused an upshift in the d-band centre according to density functional theory (DFT), which enhanced the adsorption of reaction intermediates.²⁰ They prepared a FL- MoS_2 -20 catalyst with a Sv concentration of 16.3% by a chemical reduction method, which showed excellent NH_3 yield. Zhou *et al.* pointed out that the appropriate Sv concentration of MoS_2 can greatly improve its proton adsorption/desorption capacity.²¹ From theoretical and experimental results, it can be seen that strengthening Sv while maintaining the few-layer structure has the potential to achieve the enhancement of catalytic performance.

The current techniques for Sv construction primarily include plasma treatment,^{22–25} heteroatom doping,^{14,17,26–28} chemical reduction,^{21,29–31} etc., enabling precise control over the concentration of Sv. Jin *et al.* synthesized a NiS_2 catalyst by using an argon plasma etching strategy; when the concentration of Sv was 5.9%, its hydrogen evolution reaction (HER) performance was greatly improved.³² Zhou *et al.* used hydrothermal doping of copper into MoS_2 nanosheets, which doubled the number of Sv on MoS_2 , thereby increasing the STY of CO_2 hydrogenation to methanol by 2.27 times.³³ However, ion etching and heteroatom doping are relatively complex, and Ma *et al.* constructed a MoS_2 /C composite with Sv by chemical reduction, and used hydrazine hydrate to regulate the concentration of Sv to achieve efficient storage of Na^+ .³⁴ The chemical reduction method is used to post-treat the catalyst, which is easy to operate and can accurately regulate Sv. Hence, the chemical reduction method is a simple and effective strategy for constructing Sv.

In this work, a series of MoS_2 catalysts with different Sv concentrations and interlayer spacing were prepared by the chemical reduction method, and the Sv concentration in MoS_2 was regulated by changing the concentration of hydrazine hydrate. By comparing different reductants, it was found that the $\text{MoS}_2\text{--N}_2\text{H}_4\text{--4}$ catalyst had abundant Sv and large interlayer spacing. The characterization results showed that hydrazine hydrate successfully regulated both the concentration of Sv and interlayer spacing. Theoretical calculations show that the introduction of Sv can increase the electron density of Mo atoms, enhance the adsorption capacity of MoS_2 to CO_2 , and increase the methanol STY. The synergistic effect of interlayer spacing and Sv plays a momentous role in tuning the activity of MoS_2 .

2 Experimental

2.1 Preparation of catalysts

Initially, 3 mmol of sodium molybdate (Na_2MoO_4) and 3 mmol of thioacetamide (TAA) were dissolved in 60 mL of deionized water. The resultant mixture was vigorously stirred for one hour and then transferred to a polytetrafluoroethylene (PTFE)-lined stainless steel high-pressure reactor. Subsequently, the

solution was heated to 180 °C and maintained at this temperature for 24 hours. Upon cooling to room temperature, the precipitate was repeatedly washed with water and ethanol, and the resultant black precipitate was collected using centrifugation at 5000 rpm. Then, the collected material was vacuum-dried overnight at 70 °C, resulting in the MoS_2 sample. Subsequently, X mL ($X = 2, 4$, and 8) of $\text{N}_2\text{H}_4\text{--H}_2\text{O}$ was added to 100 mg of the MoS_2 sample. The reaction lasted for 3 hours, leading to different Sv concentrations, denoted as $\text{MoS}_2\text{--N}_2\text{H}_4\text{--}X$ ($X = 2, 4$, and 8). $\text{MoS}_2\text{--NH}_3$ and $\text{MoS}_2\text{--NaBH}_4$ were produced by the same procedure except using the corresponding reductants ($\text{NH}_3\text{--H}_2\text{O}$ and NaBH_4). A detailed list of the materials, measurements, and calculation parameters are provided in the ESI.[†]

2.2 DFT calculations

See the ESI[†] for specific information on model building and calculations.

3 Results and discussion

3.1 Structural and morphological properties of MoS_2 after reductant treatment

The preparation route of MoS_2 materials treated with different reductants is presented in Fig. 1a. During the progression of the hydrothermal reaction, the molybdenum source and sulfur sources react to generate MoS_2 . Three different reductants ($\text{N}_2\text{H}_4\text{--H}_2\text{O}$, $\text{NH}_3\text{--H}_2\text{O}$, and NaBH_4) were used to post-process MoS_2 based on their different chemical reduction and molecular intercalation abilities to obtain MoS_2 samples with varying interlayer spacing and Sv concentrations.

The composition of the sample was analyzed by X-ray diffraction (XRD) and the resulting XRD data were compared with the standard spectra of 2H- MoS_2 . As shown in Fig. 1b and S1,[†] all diffraction peaks were observed to coincide with those

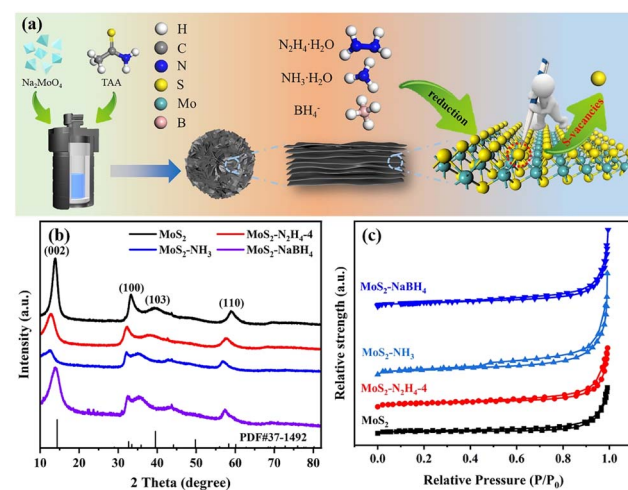


Fig. 1 (a) Sketch of preparation of MoS_2 with varying interlayer spacing and Sv concentrations via the chemical reduction method. (b) XRD patterns and (c) N_2 adsorption–desorption isotherms of MoS_2 , $\text{MoS}_2\text{--NH}_3$, $\text{MoS}_2\text{--N}_2\text{H}_4\text{--}4$ and $\text{MoS}_2\text{--NaBH}_4$ catalysts.

of 2H-MoS₂, indicating that the MoS₂ phase was successfully prepared in the sample. Upon chemical reduction, the XRD spectra of all samples revealed diffraction peaks characteristic of MoS₂, which were observed to be consistent with the peak positions documented in PDF-37-1492. Specifically, the diffraction peaks at approximately 33.5° and 58.3° corresponded to the (100) and (110) planes, respectively, while the most prominent peak of the (002) plane was located at 14.3°. Observably, the peak intensity of the (002) crystal plane decreased for all three catalysts, and the peak intensity of MoS₂-NH₃ was the lowest, which was theoretically attributed to the monolayer or the few-layer structure of MoS₂.³⁵ Interestingly, with the increase of hydrazine hydrate addition, the (002) reflection peak of MoS₂-N₂H₄-8 appeared to be almost unidentifiable, indicating the stacking of only a few MoS₂ layers in the *c*-direction. Furthermore, no additional peaks were observed after chemical reduction treatment, demonstrating that the chemical reduction reaction utilizing reductants did not produce other phases or alter the crystal structure.⁷⁷

N₂ adsorption/desorption experiments were carried out at 77 K to investigate the pore properties and specific surface area of the prepared catalyst. As shown in Fig. 1c and S2,[†] N₂ physisorption isotherms indicated that these samples all exhibit typical type-IV curves and a distinct H3-type hysteresis loop, a distinctive characteristic of mesoporous materials. The Brunauer-Emmett-Teller (BET) specific surface areas of MoS₂, MoS₂-N₂H₄-4, MoS₂-NH₃ and MoS₂-NaBH₄ were determined to be 16.1, 26.1, 37.5 and 26.5 m² g⁻¹ (Table S1[†]), respectively, indicating an increased specific surface area after chemical treatment.

To determine whether the reduction by the three reductants has disrupted the original morphology, all the samples were observed under an electron microscope (SEM) (Fig. 2a1-d1 and S3[†]). Overall, all the samples were spherical in shape, composed of tiny nanosheets forming a nanoflower morphology, with particle diameters ranging from 300 nm to 500 nm, and their appearance remained unchanged following the chemical reduction reaction with hydrazine hydrate. The well-defined structure with a nanoflower was further confirmed by the TEM technique (Fig. 2a2-d2). Moreover, the sample exhibits stacked spheres with a diameter of approximately 300–350 nm. There were many transparent layers in the nanoflower of MoS₂-N₂H₄-4 and MoS₂-NH₃, which confirmed that the two catalysts had fewer layers, consistent with the results of XRD analysis. In addition, the high-resolution transmission electron microscopy (HRTEM) images (Fig. 2a3-d3) showed a typical lamellar structure with a well-resolved *d*-spacing. It can be clearly seen that the original MoS₂ nanoflower has more edges that exhibit a layer-to-layer spacing value of 0.64 nm, which is consistent with the XRD results. Besides, there are lattice fringes observed in the MoS₂-N₂H₄-4 and MoS₂-NH₃ nanostructures that correspond to the (002) plane of MoS₂ with an enlarged interlayer spacing of 0.74 nm. This is because the intercalation of ammonium expands the interlayer spacing of MoS₂ during synthesis, thus favoring the exposure of more active sites.^{36,37} In contrast, sodium borohydride has a lower reducing ability. The layer spacing does not change and remained at 0.64 nm.

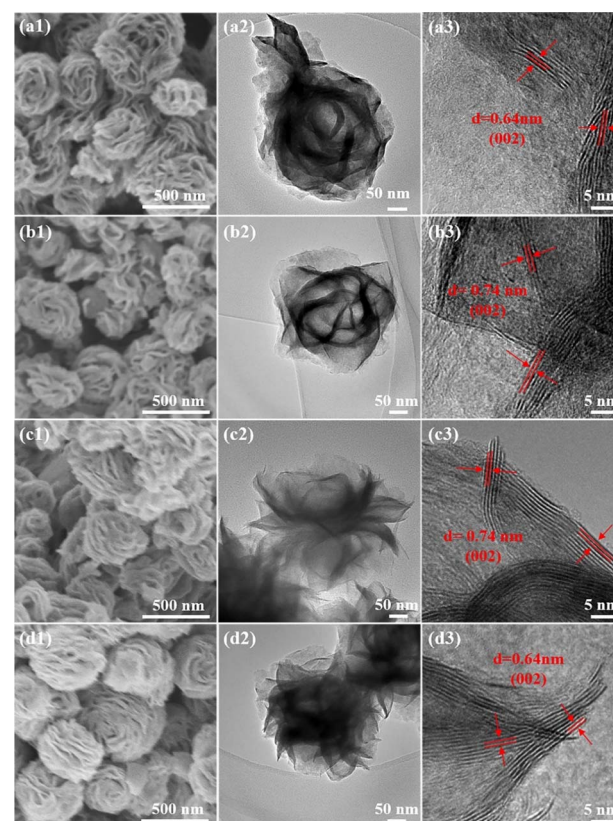


Fig. 2 (a1-d1) SEM, (a2-d2) TEM and (a3-d3) HRTEM images of (a1–a3) MoS₂, (b1–b3) MoS₂-N₂H₄-4, (c1–c3) MoS₂-NH₃ and (d1–d3) MoS₂-NaBH₄ catalysts.

The *d*(002) of MoS₂ was analyzed and measured using Bragg's law ($2d \sin \theta = n\lambda$) for XRD data (Fig. 1b and S4[†]). The calculation results (Table S1[†]) show that the *d*(002) of MoS₂-N₂H₄-4 is close to that of MoS₂-NH₃ and larger than that of MoS₂ and MoS₂-NaBH₄, which is consistent with the TEM test results.

3.2 Sulfur vacancy of MoS₂ after reductant treatment

To investigate the sulfur vacancies after reductant treatment, X-ray photoelectron spectroscopy (XPS) was utilized to study the chemical state and electronic structure of the different samples (Fig. 3). From the survey spectrum (Fig. 3a and S5[†]), it can be determined that all samples contain Mo and S elements. In Fig. 3b, the two peaks at 229.5 and 232.5 eV correspond to the 3d_{5/2} and 3d_{3/2} of Mo, while the short peak at 226.6 eV represents the 2 s electron of S. Specifically, the 3d peak of Mo can be resolved into two components, Mo⁴⁺ and Mo^{δ+}.^{19,38} According to the spectrogram, after chemical reduction treatment, the Mo^{δ+} content of all catalysts was significantly higher than that of common MoS₂, showing more Sv, because the small shoulder observed near Mo^{δ+} ($\delta < 4$) with low binding energy was due to the formation of Mo sites with unsaturated ligands.³⁹ According to the ratio of the Mo^{δ+} peak area, the order of Sv concentration can be determined as: MoS₂-NaBH₄ > MoS₂-N₂H₄-4 > MoS₂-NH₃ > MoS₂. And the Mo characteristic peak shifted towards

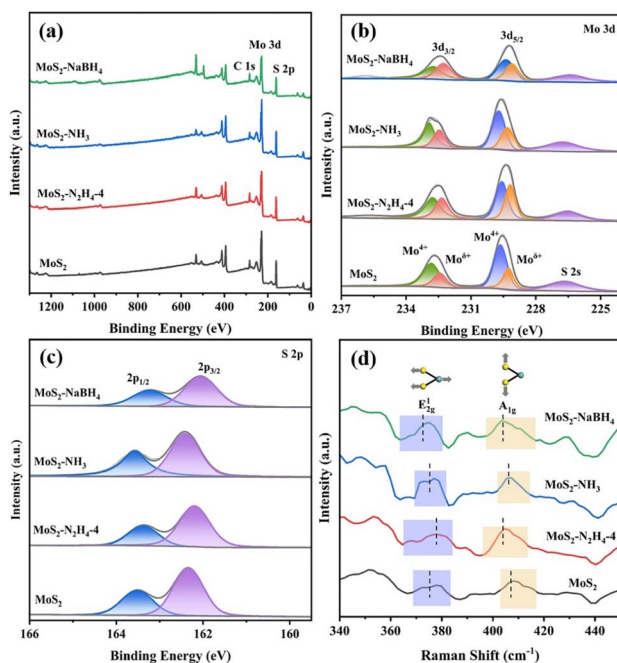


Fig. 3 (a) The XPS survey spectra and XPS spectra of (b) Mo 3d and (c) S 2p states in MoS₂, MoS₂-N₂H₄-4, MoS₂-NH₃ and MoS₂-NaBH₄ catalysts. (d) Raman spectra of MoS₂, MoS₂-N₂H₄-4, MoS₂-NH₃ and MoS₂-NaBH₄ catalysts.

lower binding energy. Despite its abundant sulfur vacancies, MoS₂-NaBH₄ was the worst performing in CO₂ hydrogenation to methanol. Thus, having sulfur vacancies alone does not increase methanol production.

It was validated that Sv concentration can be further increased by chemical reduction treatment with hydrazine hydrate. According to Fig. 3b and S6a,[†] it can be found that with the increase of the dosage of hydrazine hydrate, the characteristic Mo peak moves towards lower binding energy and the Mo^{δ+} peak area increases, which may be due to the reduction of hydrazine hydrate. In the S 2p XPS spectra of all the samples (Fig. 3c), the two peaks of S 2p_{3/2} and S 2p_{1/2} at 162.2 and 163.4 eV can be clearly distinguished in MoS₂. Compared with the S 2p XPS spectra of MoS₂, MoS₂-N₂H₄-4 and MoS₂-NaBH₄ sample characteristic peak shift occurs, and this may be related to the generation of Sv.⁴⁰ In contrast, ammonia liquor can only expand the interlayer spacing, and the two peaks of S 2p did not change. In addition, significant peak shifts were also observed in the S 2p XPS spectra of MoS₂-N₂H₄-2 and MoS₂-N₂H₄-8 (Fig. S6b[†]). With the increase of hydrazine hydrate addition, the peak shift was more obvious, indicating the presence of more Sv.^{41,42}

The structural characteristics of Sv in these catalysts were investigated by Raman spectroscopy in this experiment. As shown in Fig. 3d, all samples exhibited the main characteristic Raman vibration peaks of MoS₂ at 360–420 cm⁻¹, corresponding to the in-plane Mo-S phonon mode (E_{2g}¹) and out-of-plane Mo-S mode (A_{1g}), respectively.^{43,44} The A_{1g} and E_{2g}¹ vibration modes have changed for the expanded interlayer MoS₂ materials as compared to MoS₂.⁴⁵ In detail, the A_{1g} peaks blue shift

from 408.2 cm⁻¹ for MoS₂ to 404.4 cm⁻¹ for MoS₂-N₂H₄-4 and to 406 cm⁻¹ for MoS₂-NH₃ and to 405.4 cm⁻¹ for MoS₂-NaBH₄, while the E_{2g}¹ peaks shift from 376 cm⁻¹ for MoS₂ to 378.2 cm⁻¹ for MoS₂-N₂H₄-4 and to 375 cm⁻¹ for MoS₂-NH₃ and to 373 cm⁻¹ for MoS₂-NaBH₄. It was worth noting that the E_{2g}¹ and A_{1g} peak spread of MoS₂-N₂H₄-4 and MoS₂-NaBH₄ was wider than that of MoS₂. This is due to the Sv perturbation in the 2H lattice resulting in the reduction of the Mo-S bond and the weakening of the energy of the vibration mode, resulting in the melting of the Mo-S phonon mode in the principal plane.^{46–48} The above results are in agreement with our results using the XPS method. In addition, the distance between the E_{2g}¹ and A_{1g} peaks of MoS₂-N₂H₄-4 and MoS₂-NH₃ was reduced, indicating a diminished interaction between adjacent MoS₂ layers, because the interlayer spacing of MoS₂-N₂H₄-4 and MoS₂-NH₃ was expanded compared to the original MoS₂. MoS₂-N₂H₄-2 and MoS₂-N₂H₄-8 also conform to the above rules (Fig. S7[†]); with the increase of the amount of hydrazine hydrate, the peak position is shifted, and the peak spread becomes wider, indicating that the Sv concentration increases (Table 1).⁴⁹

In order to visually demonstrate the concentration changes of Sv in catalysts, MoS₂, MoS₂-N₂H₄, MoS₂-NH₃, and MoS₂-NaBH₄ were characterized by electron paramagnetic resonance (EPR).^{50–53} The signal at ~330 mT ($g = 2.0$) in Fig. S8[†] indicated the concentration of unsaturated sites with unpaired electrons, which is proportional to the Sv in the sample. The analysis of the data revealed that original MoS₂ exhibited some EPR signals, indicating that the MoS₂ catalyst can generate some Sv after H₂ activation. MoS₂-NaBH₄ exhibited the highest EPR signal, suggesting the strongest charge compensation effect and thus the highest Sv concentration. However, this contradicts the significant increase in methanol production with increasing Sv. This phenomenon is attributed to the change in the nature of the defects. Under the appropriate reducing agent's reduction ability, “point” defects are formed. Excessive reduction ability causes S atoms to detach, resulting in larger defects,^{54,55} and exposed edge S vacancies are not conducive to methanol production. Additionally, the peak area and intensity of MoS₂-N₂H₄ were significantly higher than those of MoS₂ and MoS₂-NH₃, indicating that MoS₂ expands the interlayer spacing while undergoing reduction, leading to more sulfur vacancies. Therefore, both the reducing ability of the reducing agent and the enlargement of the interlayer distance contribute to increasing the number of Sv. Combining TEM, XPS and EPR test results, it is found that the enriched Sv may also contribute to the enlarged interlayer spacing.

To summarize, N₂H₄·H₂O, NH₃·H₂O and NaBH₄ treatments all lead to changes in the original MoS₂ in terms of the structure, morphology and sulfur vacancies. But the effects are different due to their distinct chemical reduction and interlayer expansion capabilities. In short, NaBH₄ can lead to the enhancement of sulfur vacancies but did not expand the interlayer spacing substantially. NH₃·H₂O expands the interlayer spacing but did not lead to the enhancement of sulfur vacancies due to its lack of reducing capabilities. Meanwhile, N₂H₄·H₂O leads to both enhanced sulfur vacancies and increased interlayer spacing. The effects of these structure,

Table 1 Sulfur vacancy concentration and distance between the E_{2g}^1 and A_{1g} peaks of MoS_2 , $\text{MoS}_2\text{-N}_2\text{H}_4\text{-4}$, $\text{MoS}_2\text{-NH}_3$ and $\text{MoS}_2\text{-NaBH}_4$ catalysts

Catalysts	Sulfur vacancy concentration ^a : $\text{Mo}^{\delta+}/\text{Mo}^{4+}$ (%)	Distance between E_{2g}^1 and A_{1g} peaks ^b (cm ⁻¹)
MoS_2	47.3	32.2
$\text{MoS}_2\text{-N}_2\text{H}_4\text{-4}$	78.9	26.2
$\text{MoS}_2\text{-NH}_3$	59.4	31.0
$\text{MoS}_2\text{-NaBH}_4$	83.5	32.4

^a Calculated from XPS data. ^b Calculated from Raman data.

morphology and sulfur vacancy changes will be elaborated in the following section.

3.3 Catalytic performance evaluation for CO_2 hydrogenation

To illustrate the advantage of the synergistic effect between the interlayer spacing and sulfur vacancies, the MoS_2 catalysts and three catalysts treated with chemical reduction were initially compared through the reaction of CO_2 hydrogenation over a temperature range of 180–260 °C at a gaseous hourly space velocity (GHSV) of 8000 mL g_{cat}⁻¹ h⁻¹. Within this reaction system, methanol was the desired product, and CO and CH_4 were identified as by-products in all tested scenarios. Fig. 4 shows the CO_2 space-time yield of methanol (STY_{CH₃OH}), conversion, and methanol selectivity on MoS_2 , $\text{MoS}_2\text{-N}_2\text{H}_4\text{-4}$, $\text{MoS}_2\text{-NH}_3$ and $\text{MoS}_2\text{-NaBH}_4$ catalysts. It can be seen from Fig. 4a that under the same reaction conditions, $\text{MoS}_2\text{-N}_2\text{H}_4\text{-4}$ has the best performance. Under the optimal reaction conditions, at 220 °C, the STY_{CH₃OH} of the $\text{MoS}_2\text{-N}_2\text{H}_4\text{-4}$ catalyst can reach 0.1214 g g_{cat}⁻¹ h⁻¹, the CO_2 conversion rate is 5.52%, and

the methanol selectivity is 76.8%. The STY_{CH₃OH} of the $\text{MoS}_2\text{-N}_2\text{H}_4\text{-4}$ catalyst is 2.43 times higher than that of the MoS_2 catalyst, and the optimal temperature is 20 °C lower. This is because $\text{MoS}_2\text{-N}_2\text{H}_4\text{-4}$ has the highest methanol selectivity and high CO_2 conversion at any reaction temperature (Fig. 4b and c), which confirmed that the Sv can indeed improve the performance of the catalyst. At low temperature (180 °C), the $\text{MoS}_2\text{-NH}_3$ catalyst exhibits excellent methanol properties. Under the same reaction conditions, at 200 °C, the STY_{CH₃OH} of the $\text{MoS}_2\text{-NH}_3$ catalyst can reach 0.0772 g g_{cat}⁻¹ h⁻¹, the CO_2 conversion rate is 3.65%, and the methanol selectivity is 73.99%. However, as the temperature increased (>200 °C), the methanol production began to decline, and beyond 240 °C, the performance of the catalyst was not even as good as that of the original MoS_2 . This may be attributed to the fact that although the CO_2 conversion rate increased with the increase of temperature, which was comparable to that of $\text{MoS}_2\text{-N}_2\text{H}_4\text{-4}$, the methanol selectivity decreased, resulting in methane becoming the main product. This may be because the active sites exposed by the catalyst are the edge sulfur vacancies. The results in Fig. 4 show that the methanol yield, CO_2 conversion and methanol selectivity of the $\text{MoS}_2\text{-NaBH}_4$ catalyst are lower than those of the original MoS_2 catalyst. This may be because the reducibility of sodium borohydride is too strong, which leads to a decrease in the dissociation ability of MoS_2 to hydrogen. Some studies have shown that the CO_2 conversion is not only related to the catalyst's ability to activate CO_2 , but also related to the catalyst's ability to activate H_2 .² When CO_2 was adsorbed to the surface of the catalyst and CO was produced, due to the lack of sufficient hydrogen ions for the hydrogenation reaction, CO cannot be further reduced and was desorbed, so the main product of the $\text{MoS}_2\text{-NaBH}_4$ catalyst was CO. According to the experimental results, with the increase of reaction temperature, the CO_2 conversion increases, but the selectivity of methanol decreases. This phenomenon can be attributed to the exothermic nature of the methanol production reaction ($\text{CO}_2 + \text{H}_2 \rightarrow \text{CH}_3\text{OH} + \text{H}_2\text{O}$, $\Delta\hat{H}_{298\text{ K}} = -49.5\text{ kJ mol}^{-1}$), so it has obvious disadvantages in thermodynamics at high temperature. Alternatively, with the increase of reaction temperature, the improved CO selectivity is related to the reverse water–gas shift reaction (RWGS, $\text{CO}_2 + \text{H}_2 \rightarrow \text{CO} + \text{H}_2\text{O}$, $\Delta\hat{H}_{298\text{ K}} = 41.2\text{ kJ mol}^{-1}$), which is a main side reaction of CO_2 hydrogenation. It was also found that the best reaction temperature of $\text{MoS}_2\text{-NaBH}_4$ catalysts was 240 °C, lower than that of the original MoS_2 . The decrease of the optimal reaction temperature of the MoS_2 catalyst may be related to the expansion of MoS_2 interlayer spacing.

According to the above performance comparison, it is found that hydrazine hydrate treated MoS_2 has the best performance. Therefore, the added amount of hydrazine hydrate was optimized, and the optimized results are shown in Fig. S9 and S10.† Under the conditions of 4 MPa, 220 °C and GHSV = 8000 mL g_{cat}⁻¹ h⁻¹, the methanol STY initially increased with the increase of the addition of hydrazine hydrate, and when the addition of hydrazine hydrate reached a certain amount (4 mL), the performance of the catalyst was stable and no longer increased, which indicated that the performance of the catalyst may be limited by other factors. After analysis, it was found that

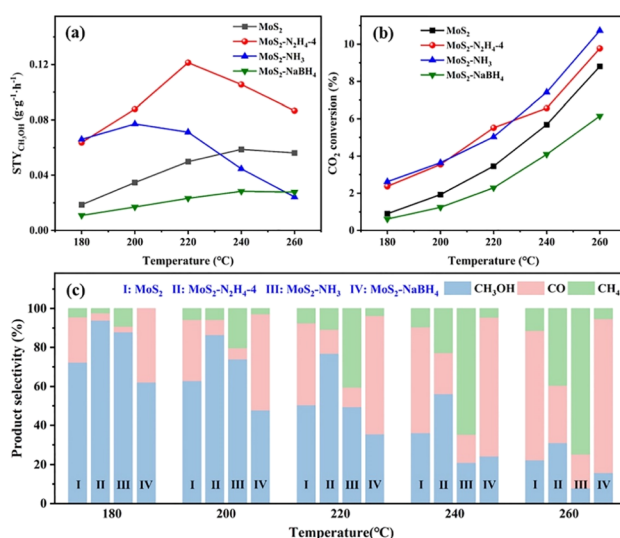


Fig. 4 (a) STY of CH_3OH and (b) CO_2 conversion on MoS_2 , $\text{MoS}_2\text{-N}_2\text{H}_4\text{-4}$, $\text{MoS}_2\text{-NH}_3$ and $\text{MoS}_2\text{-NaBH}_4$ catalysts. (c) Product selectivity of MoS_2 , $\text{MoS}_2\text{-N}_2\text{H}_4\text{-4}$, $\text{MoS}_2\text{-NH}_3$ and $\text{MoS}_2\text{-NaBH}_4$ catalysts. Reaction conditions: $V_{\text{CO}_2/\text{H}_2} = 1/3$, GHSV = 8000 mL g_{cat}⁻¹ h⁻¹, and $P = 4.0\text{ MPa}$.

$\text{MoS}_2\text{-N}_2\text{H}_4\text{-2}$, $\text{MoS}_2\text{-N}_2\text{H}_4\text{-2}$ and $\text{MoS}_2\text{-N}_2\text{H}_4\text{-8}$ had similar product selectivity, but $\text{MoS}_2\text{-N}_2\text{H}_4\text{-2}$ had lower CO_2 conversion, resulting in lower performance. In contrast, the CO_2 conversion rates of $\text{MoS}_2\text{-N}_2\text{H}_4\text{-4}$ and $\text{MoS}_2\text{-N}_2\text{H}_4\text{-8}$ were almost equal. In conclusion, the addition amount of hydrazine hydrate can affect the conversion rate of CO_2 , but its effect gradually decreases after reaching a certain amount. Therefore, $\text{MoS}_2\text{-N}_2\text{H}_4\text{-4}$ is considered to be the most appropriate catalyst for the addition of hydrazine hydrate.

The influence of GHSV was also investigated using the $\text{MoS}_2\text{-N}_2\text{H}_4\text{-4}$ catalyst at 220 °C (Fig. 5a). As the GHSV increased, the conversion of CO_2 decreased, while the selectivity of methanol and $\text{STY}_{\text{CH}_3\text{OH}}$ increased. This indicates that at high GHSV, the residence time of the reactants is short and the RWGS reaction is limited. When the reaction pressure increases from 3 MPa to 5 MPa, both CO_2 conversion and methanol selectivity are improved (Fig. S11†). Considering the CO_2 conversion rate and the mild experimental conditions, we determined the optimized GHSV of 8000 mL $\text{g}_{\text{cat}}^{-1} \text{h}^{-1}$ and pressure of 4 MPa, as the basis for this study. According to the Arrhenius formula, the apparent activation energy (E_a) of the three catalysts ($\text{MoS}_2\text{-N}_2\text{H}_4$, $\text{MoS}_2\text{-NH}_3$, and $\text{MoS}_2\text{-NaPH}_4$) was calculated (Fig. S12†), and the results showed that $\text{MoS}_2\text{-N}_2\text{H}_4$ had the lowest E_a , indicating that it had the greatest advantage in reaction kinetics. However, $\text{MoS}_2\text{-NaPH}_4$ has the lowest E_a and the slowest reaction rate, which conforms to the performance law.

The long-term stability of the $\text{MoS}_2\text{-N}_2\text{H}_4\text{-4}$ catalyst was tested for a total of 200 h at 220 °C (Fig. 5b). In the initial phase of CO_2 conversion using the $\text{MoS}_2\text{-N}_2\text{H}_4\text{-4}$ catalyst, the CO_2 conversion and methanol selectivity showed a slow upward trend and stabilized at about 5.8% and 77%, respectively, after 20 hours. This suggests that the reducing environment of the reaction contributes to Sv formation. As the reaction time was

extended to 200 h, the CO_2 conversion rate, methanol selectivity and $\text{STY}_{\text{CH}_3\text{OH}}$ showed no sign of weakening, indicating that $\text{MoS}_2\text{-N}_2\text{H}_4\text{-4}$ possesses excellent stability. According to the SEM results (Fig. S13†), the nanoflower structure of $\text{MoS}_2\text{-N}_2\text{H}_4\text{-4}$ remained good after long-term testing. The XRD pattern of the catalyst after the reaction (Fig. S14†) shows that the diffraction peak is almost the same as that of the fresh catalyst before the test, which proves that the $\text{MoS}_2\text{-N}_2\text{H}_4\text{-4}$ catalyst has excellent structural stability. Comparing the XPS spectra of the catalyst $\text{MoS}_2\text{-N}_2\text{H}_4\text{-4}$ before and after the reaction (Fig. S15†), it was found that the proportion of the Mo^{6+} peak area increased slightly, confirming that the reducing environment has increased Sv , consistent with the long-term stability performance test (Fig. 5b). The comparison of $\text{MoS}_2\text{-N}_2\text{H}_4\text{-4}$ catalysts with reported methanol synthesis (Table S2†) showed that the prepared catalysts in this study have good CO_2 hydrogenation performance.

The CO_2 -TPD technique was used to compare the CO_2 adsorption capacity of all catalysts to explain the increased catalytic activities. To elucidate the reasons for the change of the CO_2 conversion rate, the CO_2 desorption peak in the 200–500 °C region was analysed, and the results are shown in Fig. 5c and S16.† It was found that the peak area of the catalyst decreased successively: $\text{MoS}_2\text{-N}_2\text{H}_4\text{-4} > \text{MoS}_2\text{-NH}_3 > \text{MoS}_2 > \text{MoS}_2\text{-NaBH}_4$, which was consistent with the trend of the CO_2 conversion rate in Fig. 4b. Therefore, the high CO_2 conversion rate of the $\text{MoS}_2\text{-N}_2\text{H}_4\text{-4}$ catalyst was due to the production of a large number of alkaline sites, which may be caused by the Sv of the catalyst, indicating that the reduction of hydrazine hydrate can enhance the adsorption capacity of CO_2 . The CO_2 adsorption peak of the $\text{MoS}_2\text{-NaBH}_4$ catalyst appears last, indicating that the $\text{MoS}_2\text{-NaBH}_4$ catalyst had the weakest CO_2 adsorption/activation capacity. It can be seen that the reductant with stronger reducing capacity is not more favorable to the CO_2 hydrogenation reaction. In addition, with the increase of hydrazine hydrate addition, the CO_2 adsorption area of $\text{MoS}_2\text{-N}_2\text{H}_4\text{-2}$ and $\text{MoS}_2\text{-N}_2\text{H}_4\text{-8}$ also gradually expanded (Fig. S16†).

The structure–performance relationship of MoS_2 treated with different chemical agents is summarized in Fig. 5d, where expanded interlayer spacing and enhanced sulfur vacancies lead to the highest methanol STY . It can also be inferred that by increasing Sv concentration and interlayer spacing, the adsorption of CO_2 can be promoted, and the conversion rate of CO_2 can be improved. $\text{MoS}_2\text{-N}_2\text{H}_4$ can release NH_4^+ to expand the interlayer spacing, and the reducing agent is more conducive to enter the interlayer for reduction, resulting in in-plane Sv , thereby increasing the methanol yield. The methanol yield of expanding the interlayer spacing alone or increasing the Sv alone is lower than that of the combination of the two. Therefore, there is a synergistic effect between the interlayer spacing and the Sv .

3.4 Density functional theory studies

Density functional theory (DFT) was employed to investigate pristine MoS_2 and $\text{MoS}_2\text{-Sv}$, focusing on the impact of S vacancies on the adsorption of CO_2 in the context of CO_2

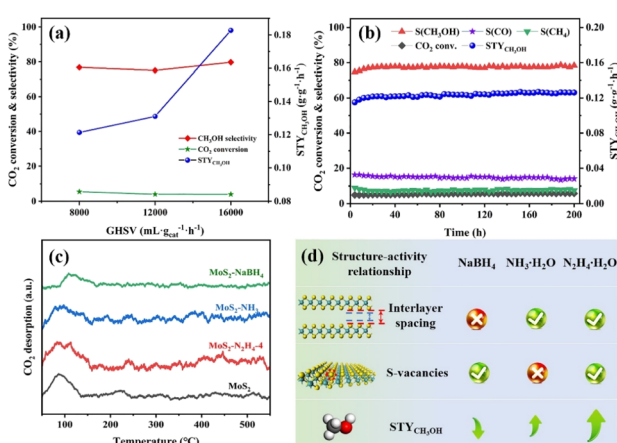


Fig. 5 (a) Effect of GHSV on CO_2 hydrogenation over the $\text{MoS}_2\text{-N}_2\text{H}_4\text{-4}$ catalyst. Reaction conditions: $T = 220$ °C, $V_{\text{CO}_2/\text{H}_2} = 1/3$, and $P = 4.0$ MPa. (b) Long-term test of the $\text{MoS}_2\text{-N}_2\text{H}_4\text{-4}$ catalyst. Reaction conditions: $T = 220$ °C, $V_{\text{CO}_2/\text{H}_2} = 1/3$, GHSV = 8000 mL $\text{g}_{\text{cat}}^{-1} \text{h}^{-1}$, and $P = 4.0$ MPa. (c) CO_2 -TPD profiles of MoS_2 , $\text{MoS}_2\text{-N}_2\text{H}_4\text{-4}$, $\text{MoS}_2\text{-NH}_3$ and $\text{MoS}_2\text{-NaBH}_4$ catalysts. (d) Structure–activity relationship diagram between different chemical reductants and the STY , interlayer spacing and sulfur vacancies of MoS_2 .

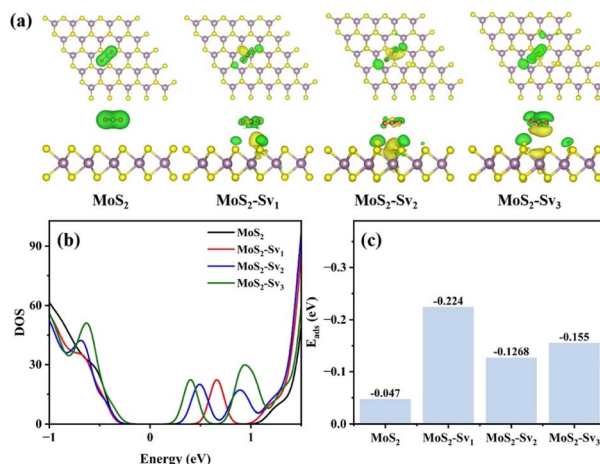


Fig. 6 (a) DFT calculated charge density difference diagrams of CO₂ adsorption, (b) total density of states, and (c) adsorption energy (E_{ads}) of CO₂.

hydrogenation to methanol. The DFT models constructed were MoS₂, MoS₂-Sv₁, MoS₂-Sv₂, and MoS₂-Sv₃ (Fig. S17 and S18†). The S-vacancy samples showed better electron transfer capacity in terms of charge density difference diagrams (Fig. 6a) during the CO₂ adsorption process compared with the vacancy-free sample. Furthermore, it was evident that an increase in sulfur vacancies results in the Mo atom gaining more electrons, leading to enhanced electron density and subsequently improving CO₂ adsorption. Based on the calculated total density of states (TDOS) (Fig. 6b), the samples with sulfur vacancies exhibited slightly smaller MoS₂ bandgaps compared to the vacancy-free sample. The increasing presence of sulfur vacancies brought the conduction band closer to the Fermi level, resulting in enhanced electron transport.³⁴ This enhancement facilitated the conversion of CO₂ into methanol and improved selectivity. The adsorption energy (E_{ads}) for CO₂ adsorption was calculated using the equation $E_{\text{ads}} = E_{\text{CO}_2+\text{surface}} - E_{\text{CO}_2} - E_{\text{surface}}$.¹³ As shown in Fig. 6c, the adsorption energy of MoS₂ with sulfur vacancies on CO₂ was significantly higher than that of the original MoS₂ catalyst, indicating that sulfur vacancies can significantly enhance the CO₂ adsorption and thus promote the CO₂ conversion.

4 Conclusions

In summary, a series of MoS₂ catalysts with different Sv concentrations and interlayer spacing were synthesized via a simple chemical reduction method. It was worth noting that when hydrazine hydrate was employed as a reductant in preparing the MoS₂-N₂H₄-4 catalyst, it not only resulted in larger interlayer spacing but also led to an increased number of sulfur vacancies. Under their combined influence, methanol STY was significantly enhanced. DFT calculations revealed that sulfur vacancies in MoS₂ increased electron density around Mo atoms, bringing them closer to the Fermi level and making active sites more reactive and catalytically efficient in CO₂ hydrogenation towards methanol production. In summary, this

work presents a new insight to resolve the reaction of MoS₂ to catalyze CO₂ valorization, highlighting its promising potential in efficient CO₂ valorization or in other catalytic systems.

Data availability

The data supporting this article have been included as part of the ESI.†

Author contributions

Langlang Qin: conceptualization, investigation, methodology, data curation, writing – original draft, validation, and visualization. Yunfei Gao: conceptualization, formal analysis, validation, supervision, writing – review & editing, and funding acquisition. Caiyun Han: writing – review & editing. Minghui Zhu: writing – review & editing. Shuang Wang: conceptualization, formal analysis, writing – review & editing, project administration, and funding acquisition.

Conflicts of interest

There are no conflicts to declare.

Acknowledgements

The present work is financially supported by the National Natural Science Foundation of China (grant numbers 22078215 and 22208104) and Research Project by Shanxi Scholarship Council of China (grant number 2021-055).

References

- 1 S. De, A. Dokania, A. Ramirez and J. Gascon, *ACS Catal.*, 2020, **10**, 14147–14185.
- 2 S.-T. Bai, G. De Smet, Y. Liao, R. Sun, C. Zhou, M. Beller, B. U. W. Maes and B. F. Sels, *Chem. Soc. Rev.*, 2021, **50**, 4259–4298.
- 3 S. Das, J. Pérez-Ramírez, J. Gong, N. Dewangan, K. Hidajat, B. C. Gates and S. Kawi, *Chem. Soc. Rev.*, 2020, **49**, 2937–3004.
- 4 C. J. Huang, S. A. Zhang, W. B. Wang, H. Z. Zhou, Z. L. Shao, L. Xia, H. Wang and Y. H. Sun, *ACS Catal.*, 2024, **14**, 1324–1335.
- 5 Y. Wang, Y. Zhu, X. Zhu, J. Shi, X. Ren, L. Zhang and S. Li, *ACS Catal.*, 2022, **13**, 714–724.
- 6 T. Biswal, K. P. Shadangi, P. K. Sarangi and R. K. Srivastava, *Chemosphere*, 2022, **298**, 134299.
- 7 R. Sen, A. Goeppert and G. K. Surya Prakash, *Angew. Chem., Int. Ed.*, 2022, **61**, e202207278.
- 8 C. F. Shih, T. Zhang, J. H. Li and C. L. Bai, *Joule*, 2018, **2**, 1925–1949.
- 9 X. H. Lin, S. B. Wang, W. G. Tu, Z. B. Hu, Z. X. Ding, Y. D. Hou, R. Xu and W. X. Dai, *Catal. Sci. Technol.*, 2019, **9**, 731–738.
- 10 Y. H. Wang, Y. Liu, L. Tan, X. H. Lin, Y. X. Fang, X. F. Lu, Y. D. Hou, G. G. Zhang and S. B. Wang, *J. Mater. Chem. A*, 2023, **11**, 26804–26811.

11 Z. D. Feng, C. Z. Tang, P. F. Zhang, K. Li, G. N. Li, J. J. Wang, Z. C. Feng and C. Li, *J. Am. Chem. Soc.*, 2023, **145**, 12663–12672.

12 S. H. Zhou, M. Kosari and H. C. Zeng, *J. Am. Chem. Soc.*, 2024, **146**, 10032–10043.

13 G. Wang, X.-L. Jiang, Y.-F. Jiang, Y.-G. Wang and J. Li, *ACS Catal.*, 2023, **13**, 8413–8422.

14 H.-Y. Su, X. Ma, C. Sun and K. Sun, *Catal. Sci. Technol.*, 2021, **11**, 3261–3269.

15 Z. F. Wang, Y. R. Kang, J. T. Hu, Q. Q. Ji, Z. X. Lu, G. L. Xu, Y. T. Qi, M. Zhang, W. W. Zhang, R. Huang, L. Yu, Z. Q. Tian and D. H. Deng, *Angew. Chem., Int. Ed.*, 2023, **62**, e202307086.

16 S. Kanuri, S. Roy, C. Chakraborty, S. P. Datta, S. A. Singh and S. Dinda, *Int. J. Energy Res.*, 2021, **46**, 5503–5522.

17 Y. Yuan, L. Qi, Z. Gao, T. Guo, D. Zhai, Y. He, J. Ma and Q. Guo, *Molecules*, 2023, **28**, 5796.

18 J. T. Hu, L. Yu, J. Deng, Y. Wang, K. Cheng, C. Ma, Q. H. Zhang, W. Wen, S. S. Yu, Y. Pan, J. Z. Yang, H. Ma, F. Qi, Y. K. Wang, Y. P. Zheng, M. S. Chen, R. Huang, S. H. Zhang, Z. C. Zhao, J. Mao, X. Y. Meng, Q. Q. Ji, G. J. Hou, X. W. Han, X. H. Bao, Y. Wang and D. H. Deng, *Nat. Catal.*, 2021, **4**, 242–250.

19 S. Zhou and H. C. Zeng, *ACS Catal.*, 2022, **12**, 9872–9886.

20 H. Fei, R. Liu, J. Wang, T. Guo, F. Liu, Z. Wu and D. Wang, *Chem. Eng. J.*, 2023, **476**, 146895.

21 Y. Zhou, C. Li, Y. Zhang, L. Wang, X. Fan, L. Zou, Z. Cai, J. Jiang, S. Zhou, B. Zhang, H. Zhang, W. Li and Z. Chen, *Adv. Funct. Mater.*, 2023, **33**, 2304302.

22 J. W. Guo, H. B. Zhao, Z. W. Yang, L. W. Wang, A. Z. Wang, J. Zhang, L. H. Ding, L. F. Wang, H. Liu and X. Yu, *Adv. Funct. Mater.*, 2024, 2315714.

23 C. Li, R. Z. Xu, S. X. Ma, Y. H. Xie, K. G. Qu, H. F. Bao, W. W. Cai and Z. H. Yang, *Chem. Eng. J.*, 2021, **415**, 129018.

24 A. Y. Lu, X. L. Yang, C. C. Tseng, S. X. Min, S. H. Lin, C. L. Hsu, H. N. Li, H. C. Idriss, J. L. Kuo, K. W. Huang and L. J. Li, *Small*, 2016, **12**, 5530–5537.

25 L. Tian, Z. J. Huang, X. H. Lu, T. J. Wang, W. J. Cheng, H. M. Yang, T. Z. Huang, T. X. Li and Z. Li, *Inorg. Chem.*, 2023, **62**, 1659–1666.

26 H. Li, L. Wang, Y. Dai, Z. Pu, Z. Lao, Y. Chen, M. Wang, X. Zheng, J. Zhu, W. Zhang, R. Si, C. Ma and J. Zeng, *Nat. Nanotechnol.*, 2018, **13**, 411–417.

27 C. H. Yan, E. S. Han, X. H. Yang, K. S. Hu, H. T. Xu, Y. D. Li, Y. Z. He and S. Lu, *Ceram. Int.*, 2023, **49**, 14155–14165.

28 S. Q. Ding, Z. J. Li, X. Dai, C. L. Sun and A. L. Meng, *Chem. Eng. J.*, 2021, **417**, 129328.

29 Y. H. Ma, D. F. Leng, X. M. Zhang, J. J. Fu, C. R. Pi, Y. Zheng, B. A. Gao, X. G. Li, N. Li, P. K. Chu, Y. S. Luo and K. F. Huo, *Small*, 2022, **18**, 2203173.

30 Z. S. Zhang, C. L. Mao, D. M. Meira, P. N. Duchesne, A. A. Tountas, Z. Li, C. Y. Qiu, S. L. Tang, R. Song, X. Ding, J. C. Sun, J. F. Yu, J. Y. Howe, W. G. Tu, L. Wang and G. A. Ozin, *Nat. Commun.*, 2022, **13**, 1512.

31 Y. Zhang, L. Ye, J. H. Guo, Y. Y. Shang, F. M. Guo, Y. J. Zhang and J. Xu, *J. Mater. Sci.*, 2021, **56**, 9368–9381.

32 J. Jin, X. Wang, Y. Hu, Z. Zhang, H. Liu, J. Yin and P. Xi, *Nano Micro Lett.*, 2024, **16**, 63.

33 S. Zhou, W. Ma, U. Anjum, M. Kosari, S. Xi, S. M. Kozlov and H. C. Zeng, *Nat. Commun.*, 2023, **14**, 5872.

34 X. Ma, L. Diao, Y. Wang, L. Zhang, Y. Lu, D. Li, D. Yang and X. She, *Chem. Eng. J.*, 2023, **457**, 141116.

35 H. F. Li, Q. Yang, F. N. Mo, G. J. Liang, Z. X. Liu, Z. J. Tang, L. T. Ma, J. Liu, Z. C. Shi and C. Y. Zhi, *Energy Storage Mater.*, 2019, **19**, 94–101.

36 J. W. Tan, W. B. A. Zhang, Y. J. Shu, H. Y. Lu, Y. Tang and Q. S. Gao, *Sci. Bull.*, 2021, **66**, 1003–1012.

37 T. L. Yan, Y. S. Jia, K. G. Hou, Q. S. Gao, Y. H. Zhang and Y. Tang, *iScience*, 2024, **27**, 109824.

38 L. Li, Z. D. Qin, L. Ries, S. Hong, T. Michel, J. Yang, C. Salameh, M. Bechelany, P. Miele, D. Kaplan, M. Chhowalla and D. Voiry, *ACS Nano*, 2019, **13**, 6824–6834.

39 R. Liu, L. N. Ma, G. D. Niu, X. L. Li, E. Y. Li, Y. Bai and G. H. Yuan, *Adv. Funct. Mater.*, 2017, **27**, 1701635.

40 F. Zhou, S. Xin, H. W. Liang, L. T. Song and S. H. Yu, *Angew. Chem., Int. Ed.*, 2014, **53**, 11552–11556.

41 P. Shen, X. C. Li, Y. J. Luo, Y. L. Guo, X. L. Zhao and K. Chu, *ACS Nano*, 2022, **16**, 7915–7925.

42 L. R. L. Ting, Y. L. Deng, L. Ma, Y. J. Zhang, A. A. Peterson and B. S. Yeo, *ACS Catal.*, 2016, **6**, 861–867.

43 T. Zhu, W. Shen, X. Y. Wang, Y. F. Song and W. Wang, *Chem. Eng. J.*, 2019, **378**, 122159.

44 G. H. Yang, L. Zhao, G. Q. Huang, Z. P. Liu, S. Y. Yu, K. W. Wang, S. S. Yuan, Q. W. Sun, X. T. Li and N. Li, *ACS Appl. Mater. Interfaces*, 2021, **13**, 21474–21481.

45 X. Li, S. Guo, J. Su, X. Ren and Z. Fang, *ACS Appl. Mater. Interfaces*, 2020, **12**, 28474–28483.

46 C. Tsai, H. Li, S. Park, J. Park, H. S. Han, J. K. Norskov, X. L. Zheng and F. Abild-Pedersen, *Nat. Commun.*, 2017, **8**, 15113.

47 C. Hu, Z. Z. Jiang, W. D. Zhou, M. M. Guo, T. Yu, X. F. Luo and C. L. Yuan, *J. Phys. Chem. Lett.*, 2019, **10**, 4763–4768.

48 P. Thangasamy, S. Oh, S. Nam and I.-K. Oh, *Carbon*, 2020, **158**, 216–225.

49 A. T. Garcia-Esparza, S. Park, H. Abroshan, O. A. P. Mellone, J. Vinson, B. Abraham, T. R. Kim, D. Nordlund, A. Gallo, R. Alonso-Mori, X. L. Zheng and D. Sokaras, *ACS Nano*, 2022, **16**, 6725–6733.

50 X. Wang, Y. Zhang, H. Si, Q. Zhang, J. Wu, L. Gao, X. Wei, Y. Sun, Q. Liao, Z. Zhang, K. Ammarah, L. Gu, Z. Kang and Y. Zhang, *J. Am. Chem. Soc.*, 2020, **142**, 4298–4308.

51 F. Wei, W. Xue, Z. Yu, X. F. Lu, S. Wang, W. Lin and X. Wang, *Chin. Chem. Lett.*, 2024, **35**, 108313.

52 Y. Liu, W. Xue, X. Liu, F. Wei, X. Lin, X. F. Lu, W. Lin, Y. Hou, G. Zhang and S. Wang, *Small*, 2024, 2402004.

53 J. W. Tan, J. J. Shao, Y. H. Shi, W. B. Zhang and Q. S. Gao, *ACS Sustainable Chem. Eng.*, 2022, **10**, 13525.

54 L. Li, Z. Qin, L. Ries, S. Hong, T. Michel, J. Yang, C. Salameh, M. Bechelany, P. Miele, D. Kaplan, M. Chhowalla and D. Voiry, *ACS Nano*, 2019, **13**, 6824–6834.

55 Y. H. Shi, W. B. Zhang, J. W. Tan, T. L. Yan, Y. S. Jia, Z. Y. Wang, Y. Tang and Q. S. Gao, *Adv. Mater. Interfaces*, 2022, **9**, 2200505.